Journal of Nonlinear Mathematical Physics (2023) 30:1134–1152
https://doi.org/10.1007/s44198-023-00115-7

RESEARCH ARTICLE

Numerical Simulation by Using the Spectral Collocation Method for Williamson Nanofluid Flow Over an Exponentially Stretching Sheet with Slip Velocity

M. M. Khader[1,2] · M. M. Babatin[1] · Ahmed M. Megahed[2]

Received: 19 December 2022 / Accepted: 24 April 2023 / Published online: 9 June 2023

Abstract

The current research examines the rate of heat and mass transfer in MHD non-Newtonian Williamson nanofluid flow across an exponentially permeable stretched surface sensitive to heat generation/absorption and mass suction. The influences of Brownian motion and thermophoresis are included. In addition, the stretched surface is subjected to an angled outside magnetic field. This study incorporates the variable viscosity, viscous dissipation, and slip velocity. The fundamental rules of motion and heat transmission have been constructed mathematically to fit the current flow problem. By using appropriate self-similarity transformations, the supplied system of PDEs is transformed into a nonlinear system of ODEs. Here, we use the spectral collocation method with the help of Vieta-Lucas polynomials approximation. This procedure converts the present model to a system of algebraic equations which is developed as a constrained optimization problem, which is then optimized to get the solution and the unknown coefficients. Calculations are made for the skin friction, wall temperature gradient, and wall concentration gradient. By comparing our findings in some special cases to those in the literature, a review of the literature confirms the results described here.

Keywords Williamson nanofluid · Aligned magnetic field · Exponential stretching · Slip velocity · Vieta-Lucas polynomials · Spectral collocation method · Optimization technique

✉ M. M. Khader
mmkhader@imamu.edu.sa

M. M. Babatin
mmbabatin@imamu.edu.sa

Ahmed M. Megahed
ahmed.abdelbaqk@fsc.bu.edu.eg

[1] Department of Mathematics and Statistics, College of Science, Imam Mohammad Ibn Saud Islamic University (IMSIU), Riyadh 11566, Saudi Arabia

[2] Department of Mathematics, Faculty of Science, Benha University, Benha, Egypt

Mathematics Subject Classification 41A30 · 65N12 · 65M60 · 76F12

1 Introduction

Non-Newtonian fluids (NNFs) are substances in which interactions between particles in the liquid phase can result in effects like shear thinning. Since NNFs are typically very non-linear PDEs, an accurate solution is typically not possible. Although non-Newtonian liquids exhibit a variety of rheological properties in nature, there is no one constitutive relationship between strain rate and stress that can be used to classify all of these qualities. Various constitutive formulations for NNFs have been developed in the literature. NNFs are of utmost importance today because of their potential application in cutting-edge technology and industry. NNFs according to the definition, do not follow Newton's laws of motion. Examples include paste, paints, food items, waste liquids, lubricants, and a wide range of other things. A significant and basic subclass of rate-type NNFs is the Maxwell model. Also, Williamson fluid is a type of NNF that exhibits shear thinning. Williamson [1] was the one who originally put forth this model. Later, this model employed by several authors ([2–4]).

A nanofluid is created when nanoparticles smaller than 100 nm are suspended in a regular base fluid ([5–8]). The word "nanofluid" was originally used by Choi [9] about three decades ago. However, nanoparticles have only lately become accessible and affordable enough to justify consideration for use in practical applications. Following the groundbreaking work of Choi, some researchers ([10–12]) have also taken into account diverse physical configurations and summarized the significance of nanofluid flow and heat transfer in numerous engineering applications.

Because of their frequent appearance in many applications in fluid mechanics, biology, physics, and engineering, PDEs have been the subject of many investigations. As a result, the solutions of ODEs of physical relevance have received a lot of attention [13]. The spectral collocation method (SCM) is a numerical approach utilized for solving ODEs. This method involves an approximation of the solution by summing up basis functions and determining their coefficients by enforcing the differential equation at a limited number of collocation points ([14, 15]). Among the variety of base functions available for use in SCM, the Vieta-Lucas polynomials (VLPs) are a set of orthogonal polynomials that can serve as effective basis functions [16]. Utilizing SCM with VLPs comes with the benefit of their remarkable convergence properties. The accuracy of the solution improves rapidly with an increase in the number of collocation points. Moreover, VLPs exhibit good stability properties, making them suitable for solving differential equations that are stiff or have rapidly varying solutions. Vieta-Lucas polynomials have the added advantage of having a closed-form expression, which simplifies their computation and manipulation. This feature can result in substantial computational savings, especially when compared to other techniques that necessitate solving extensive systems of ODEs [17].

Nonetheless, this research aims to investigate the approximate solution for the proposed problem by using SCM based on VLPs. The study's novelty and purpose stem

from the fact that it is the first of its type to use the given numerical procedure to numerically solve the proposed problem.

2 Mathematical Formulations

We take into account a nanofluid's two-dimensional non-Newtonian Williamson flow in the direction of an exponentially stretching sheet that is maintained at a constant temperature T_w and concentration C_w. Also, T_∞ and C_∞ represent the respective ambient temperature and concentration values. In this research, we take into account the slip velocity with the assumption that the sheet is rough. Figure 1 shows the problem formulation, Cartesian coordinates x and y, corresponding velocity components u and v, and the fluid flow configuration. The Williamson nanofluid is supposed to move with a velocity of $U_0 e^{\frac{x}{L}}$, where U_0 is a constant, as a result of the surface being stretched through the xy-plane. Additionally, the assumption that the sheet is permeable results in a suction velocity of v_w. These prerequisites lead to the following definitions of the primary boundary layer (BL) equations for continuity, momentum, energy, and concentration [18]:

$$\frac{\partial u}{\partial x} + \frac{\partial v}{\partial y} = 0, \tag{1}$$

$$u\frac{\partial u}{\partial x} + v\frac{\partial u}{\partial y} = \frac{1}{\rho_\infty}\frac{\partial}{\partial y}\left(\mu\frac{\partial u}{\partial y} + \mu\frac{\Gamma}{\sqrt{2}}\left(\frac{\partial u}{\partial y}\right)^2\right) - \sin^2\beta\,\frac{\sigma B_0^2}{\rho_\infty}u - \frac{\mu}{\rho_\infty k}u, \tag{2}$$

$$\begin{aligned} u\frac{\partial T}{\partial x} + v\frac{\partial T}{\partial y} &= \frac{\kappa}{\rho_\infty c_p}\frac{\partial^2 T}{\partial y^2} + \tau\left(D_B(C)\left(\frac{\partial C}{\partial y}\frac{\partial T}{\partial y}\right) + \left(\frac{D_T}{T_\infty}\right)\left(\frac{\partial T}{\partial y}\right)^2\right) \\ &+ \frac{\mu}{\rho_\infty c_p}\left(\left(\frac{\partial u}{\partial y}\right)^2 + \frac{\Gamma}{\sqrt{2}}\left(\frac{\partial u}{\partial y}\right)^3\right) + \frac{Q_0}{\rho_\infty c_p}(T - T_\infty), \end{aligned} \tag{3}$$

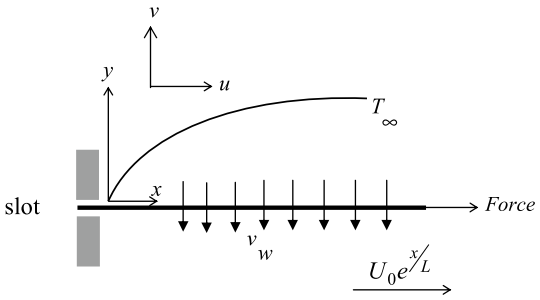

Fig. 1 Physical configuration of the problem

$$u\frac{\partial C}{\partial x}+v\frac{\partial C}{\partial y}=D_B\frac{\partial^2 C}{\partial y^2}+\frac{D_T}{T_\infty}\frac{\partial^2 T}{\partial y^2}, \tag{4}$$

where u and v represent the fluid velocity vector's x and y axis coefficients, Γ is the Williamson parameter, μ is the nanofluid dynamic viscosity, β is the inclination angle, κ is the fluid's thermal conductivity, D_B is the Brownian motion's variable diffusivity, σ is electrical conductivity, c_p is the specific heat at constant pressure, ρ_∞ is the density of the nanofluid at the ambient, B_0 is the magnetic field strength, k is the permeability of the porous medium, D_T is the coefficient of thermophoretic diffusion and Q_0 is the initial value of the heat generation coefficient. The previously mentioned governing equations have boundary conditions that take the following forms:

$$u=U_w+\frac{\lambda_1}{\mu_\infty}\left(\mu\frac{\partial u}{\partial y}+\mu\frac{\Gamma}{\sqrt{2}}\left(\frac{\partial u}{\partial y}\right)^2\right),\quad v=-v_w,\quad T=T_w,\quad C=C_w,\quad at\quad y=0, \tag{5}$$

$$u\to 0,\qquad T\to T_\infty,\qquad C\to C_\infty,\qquad as\quad y\to\infty, \tag{6}$$

where λ_1 is the slip velocity factor and μ_∞ is the ambient nanofluid viscosity. According to analysis, Megahed's previously described nonlinear temperature-dependent nanofluid viscosity is as follows [19]:

$$\mu(T)=\mu_\infty e^{-\alpha\theta(\eta)}, \tag{7}$$

where α is the viscosity parameter.

Non-linear PDEs make up the governing Eqs. (1) through (4). These nonlinear PDEs are translated into nonlinear ODEs using the dimensionless transformation described below:

$$\eta=y\sqrt{\frac{U_0\rho_\infty}{2L\mu_\infty}}e^{\frac{x}{2L}},\qquad u=U_0e^{\frac{x}{L}}f'(\eta),\qquad v=-\sqrt{\frac{U_0\mu_\infty}{2L\rho_\infty}}e^{\frac{x}{2L}}\left(f(\eta)+\eta f'\right), \tag{8}$$

$$T=T_\infty+(T_w-T_\infty)\theta(\eta),\qquad C=C_\infty+(C_w-C_\infty)\phi(\eta). \tag{9}$$

Given the previously indicated suitable dimensionless relationships, it is shown that the controlling model for the problem is an innovative system of high nonlinear, multi-degree ODEs as regards:

$$\left(\left(1+W_e f''\right)f'''-\alpha\theta' f''\left(1+0.5\,W_e f''\right)\right)e^{-\alpha\theta}+ff''-2f'^2-(M\sin^2\beta)f'-Ke^{-\alpha\theta}f'=0, \tag{10}$$

$$\frac{1}{Pr}\theta''+f\theta'-f'\theta+Nt\left(\theta'\right)^2+Nb\theta'\phi'+Ecf''^2\left(1+0.5\,W_e f''\right)e^{-\alpha\theta}+Q\theta=0, \tag{11}$$

$$\phi''+Scf\phi'+\frac{Nt}{Nb}\theta''=0, \tag{12}$$

under the corresponding boundary constraints:

$$f'(0) = 1 + \lambda f'' \left(1 + 0.5\, W_e f''\right) e^{-\alpha\theta(0)}, \qquad f(0) = \gamma, \qquad \theta(0) = 1, \quad \phi(0) = 1, \tag{13}$$

$$f'(\infty) \to 0, \qquad \theta(\infty) \to 0, \qquad \phi(\infty) \to 0. \tag{14}$$

The Williamson parameter, magnetic number, porous parameter, Prandtl number, thermophoresis parameter, Brownian motion parameters, and Eckert number, respectively, as well as the heat source parameter are represented by the dimensionless parameters that are found in the controlling equations above. These terms are defined as follows, respectively:

$$W_e = \left(\frac{U_0}{2}\right)^{\frac{2}{3}} \frac{\Gamma}{\sqrt{L}} e^{\frac{x}{2L}}, \qquad M = \frac{\sigma B_0}{\rho_\infty U_0} e^{\frac{-x}{L}}, \qquad K = \frac{\nu_\infty L}{k U_0} e^{\frac{-x}{L}}, \qquad Pr = \frac{\mu_\infty c_p}{\kappa},$$
$$Nt = \frac{\tau D_T \left(T_w - T_\infty\right)}{\nu_\infty T_\infty}, \quad Nb = \frac{\tau D_B \left(C_w - C_\infty\right)}{\nu_\infty}, \quad Ec = \frac{U_0^2}{(T_w - T_\infty) c_p}, \quad Q = \frac{Q_0 L}{U_0 \rho_\infty c_p} e^{\frac{-x}{L}}.$$

Skin-friction coefficient (SFC), local Nusselt number (LNN), and local Sherwood number (LSN) are terms used to characterize the friction drags, heat transfer rate, and mass transfer rate, respectively, which can be introduced as follows [20]:

$$\sqrt{2} C f_x \mathrm{Re}_x^{1/2} = -f''(0)\left(1 + 0.5\, W_e f''(0)\right) e^{-\alpha\theta(0)},$$
$$\frac{1}{\sqrt{2}} \mathrm{Re}_x^{-1/2} e^{\frac{-x}{2L}} Nu_x = -\theta'(0),$$
$$\frac{1}{\sqrt{2}} \mathrm{Re}_x^{-1/2} e^{\frac{-x}{2L}} Sh_x = -\phi'(0),$$

where the local Reynolds number is $\mathrm{Re}_x = \frac{U_w L}{\nu_\infty}$.

3 Procedure of Solution

4 Approximate the Derivatives

In this subsection, we will try to generate a new family of the Vieta-Lucas polynomials as orthogonal polynomials on the interval $[0, \hbar]$, and so-called the shifted Vieta-Lucas polynomials and denoted by $\mathrm{VL}_k^s(\eta)$. This will be obtained by using the transformation $z = (4/\hbar)\eta - 2$ as follows:

$$\mathrm{VL}_k^s(\eta) = \mathrm{VL}_k((4/\hbar)\eta - 2).$$

Also, by the following recurrence relation, we can generate the shifted VLPs $\mathrm{VL}_k^s(\eta)$:

$$\mathrm{VL}^{s}_{k+1}(\eta) = ((4/\hbar)\eta - 2)\mathrm{VL}^{s}_{k}(\eta) - \mathrm{VL}^{s}_{k-1}(\eta), \qquad k = 1, 2, \dots,$$

where, $\mathrm{VL}^{s}_{0}(\eta) = 2$, $\mathrm{VL}^{s}_{1}(\eta) = (4/\hbar)\eta - 2$. It is easy to find that $\mathrm{VL}^{s}_{k}(\hbar) = (-1)^k \mathrm{VL}^{s}_{k}(0) = 2$, $k = 0, 1, 2 \dots$.

The function $\psi(\eta) \in L_2[0, \hbar]$ can be approximated as a finite series sum (the first $(m+1)$-terms) as follows:

$$\psi_m(\eta) = \sum_{\ell=0}^{m} c_\ell \, \mathrm{VL}^{s}_{\ell}(\eta). \tag{15}$$

Here we use the following approximate formula of $D^{(n)}\psi_m(\eta)$ of the approximated function $\psi_m(\eta)$ defined in the form (15) [17]:

$$\psi^{(n)}_{m}(\eta) = \sum_{j=n}^{m} \sum_{k=0}^{j-n} c_j \, \chi_{j,k,n} \, \eta^{j-k-n}, \quad \chi_{j,k,n} = \frac{(-1)^k \, 4^{j-k} (2j) \, \Gamma(2j-k) \, \Gamma(j-k+1)}{\hbar^n \Gamma(k+1) \, \Gamma(2j-2k+1) \, \Gamma(j-k+1-n)}. \tag{16}$$

For more details about the shifted VLPs and their convergence analysis of (15) and (16), see [17].

5 Procedure Solution Using SCM

We are going to use the proposed method to solve numerically the system under (10)–(14). We approximate $f(\eta)$, $\theta(\eta)$, and $\phi(\eta)$ by $f_p(\eta)$, $\theta_p(\eta)$, and $\phi_p(\eta)$, respectively in the following form:

$$f_p(\eta) = \sum_{o=0}^{p} a_o \, \mathrm{VL}^{s}_{o}(\eta), \qquad \theta_p(\eta) = \sum_{o=0}^{p} b_o \, \mathrm{VL}^{s}_{o}(\eta), \qquad \phi_p(\eta) = \sum_{o=0}^{p} c_o \, \mathrm{VL}^{s}_{o}(\eta). \tag{17}$$

By substituting (17) and the formula (16), the non-linear system Eqs. (10)–(12) will be reduced to the following form:

(18)

$$\left(1 + W_e\left(\sum_{o=2}^{p}\sum_{k=0}^{o-2} a_o \, \chi_{o,k,2} \, \eta^{o-k-2}\right)\right)\left(\sum_{o=3}^{p}\sum_{k=0}^{o-3} a_o \, \chi_{o,k,3} \, \eta^{o-k-3}\right) - \alpha\left(\sum_{o=1}^{p}\sum_{k=0}^{o-1} b_o \, \chi_{o,k,1} \, \eta^{o-k-1}\right).$$
$$\left(\sum_{o=2}^{p}\sum_{k=0}^{o-2} a_o \, \chi_{o,k,2} \, \eta^{o-k-2}\right)\left(1 + 0.5W_e\left(\sum_{o=2}^{p}\sum_{k=0}^{o-2} a_o \, \chi_{o,k,2} \, \eta^{o-k-2}\right)\right) + \left(\left(\sum_{o=0}^{p} a_o \, \mathrm{VL}^{s}_{o}(\eta)\right).\right.$$
$$\left.\left(\sum_{o=2}^{p}\sum_{k=0}^{o-2} a_o \, \chi_{o,k,2} \, \eta^{o-k-2}\right) - 2\left(\sum_{o=1}^{p}\sum_{k=0}^{o-1} a_o \, \chi_{o,k,1} \, \eta^{o-k-1}\right)^2 - M\sin^2\beta\left(\sum_{o=1}^{p}\sum_{k=0}^{o-1} a_o \, \chi_{o,k,1} \, \eta^{o-k-1}\right)\right).$$
$$\mathrm{Exp}\left(\alpha\left(\sum_{o=0}^{p} b_o \, \mathrm{VL}^{s}_{o}(\eta)\right)\right) - K\left(\sum_{o=1}^{p}\sum_{k=0}^{o-1} a_o \, \chi_{o,k,1} \, \eta^{o-k-1}\right) = 0,$$

$$\left(\frac{1}{Pr}\right)\left(\sum_{o=2}^{p}\sum_{k=0}^{o-2} b_o\,\chi_{o,k,2}\,\eta^{o-k-2}\right)+\left(\sum_{o=0}^{p} a_o\,\mathrm{VL}_o^s(\eta)\right)\left(\sum_{o=1}^{p}\sum_{k=0}^{o-1} b_o\,\chi_{o,k,1}\,\eta^{o-k-1}\right)-\left(\sum_{o=0}^{p} b_o\,\mathrm{VL}_o^s(\eta)\right).$$
$$\left(\sum_{o=1}^{p}\sum_{k=0}^{o-1} a_o\,\chi_{o,k,1}\,\eta^{o-k-1}\right)+Nt\left(\sum_{o=1}^{p}\sum_{k=0}^{o-1} b_o\,\chi_{o,k,1}\,\eta^{o-k-1}\right)^2+Nb\left(\sum_{o=1}^{p}\sum_{k=0}^{o-1} b_o\,\chi_{o,k,1}\,\eta^{o-k-1}\right).$$
$$\left(\sum_{o=1}^{p}\sum_{k=0}^{o-1} c_o\,\chi_{o,k,1}\,\eta^{o-k-1}\right)+Ec\left(\left(\sum_{o=2}^{p}\sum_{k=0}^{o-2} a_o\,\chi_{o,k,2}\,\eta^{o-k-2}\right)^2+\frac{W_e}{2}\left(\sum_{o=2}^{p}\sum_{k=0}^{o-2} a_o\,\chi_{o,k,2}\,\eta^{o-k-2}\right)^3\right).$$
$$\mathrm{Exp}\left(-\alpha\left(\sum_{o=0}^{p} b_o\,\mathrm{VL}_o^s(\eta)\right)\right)+Q\left(\sum_{o=0}^{p} b_o\,\mathrm{VL}_o^s(\eta)\right)=0. \tag{19}$$

$$\sum_{o=2}^{p}\sum_{k=0}^{o-2} c_o\,\chi_{o,k,2}\,\eta^{o-k-2}+Sc\left(\sum_{o=0}^{p} a_o\,\mathrm{VL}_o^s(\eta)\right)\left(\sum_{o=1}^{p}\sum_{k=0}^{o-1} c_o\,\chi_{o,k,1}\,\eta^{o-k-1}\right)+\frac{Nt}{Nb}\left(\sum_{o=2}^{p}\sum_{k=0}^{o-2} b_o\,\chi_{o,k,2}\,\eta^{o-k-2}\right)=0. \tag{20}$$

By collocating the previous Eqs. (18)–(20) at $p+1-n$ of nodes $_{\eta_j,\,j=0,1,\ldots,p-n}$, it will reduce to the form:

$$\left(1+W_e\left(\sum_{o=2}^{p}\sum_{k=0}^{o-2} a_o\,\chi_{o,k,2}\,\eta_q^{o-k-2}\right)\right)\left(\sum_{o=3}^{p}\sum_{k=0}^{o-3} a_o\,\chi_{o,k,3}\,\eta_q^{o-k-3}\right)-\alpha\left(\sum_{o=1}^{p}\sum_{k=0}^{o-1} b_o\,\chi_{o,k,1}\,\eta_q^{o-k-1}\right).$$
$$\left(\sum_{o=2}^{p}\sum_{k=0}^{o-2} a_o\,\chi_{o,k,2}\,\eta_q^{o-k-2}\right)\left(1+0.5W_e\left(\sum_{o=2}^{p}\sum_{k=0}^{o-2} a_o\,\chi_{o,k,2}\,\eta_q^{o-k-2}\right)\right)+\left(\left(\sum_{o=0}^{p} a_o\,\mathrm{VL}_o^s(\eta_q)\right).\right.$$
$$\left.\left(\sum_{o=2}^{p}\sum_{k=0}^{o-2} a_o\,\chi_{o,k,2}\,\eta_q^{o-k-2}\right)-2\left(\sum_{o=1}^{p}\sum_{k=0}^{o-1} a_o\,\chi_{o,k,1}\,\eta_q^{o-k-1}\right)^2-M\sin^2\beta\left(\sum_{o=1}^{p}\sum_{k=0}^{o-1} a_o\,\chi_{o,k,1}\,\eta_q^{o-k-1}\right)\right).$$
$$\mathrm{Exp}\left(\alpha\left(\sum_{o=0}^{p} b_o\,\mathrm{VL}_o^s(\eta_q)\right)\right)-K\left(\sum_{o=1}^{p}\sum_{k=0}^{o-1} a_o\,\chi_{o,k,1}\,\eta_q^{o-k-1}\right)=0, \tag{21}$$

$$\left(\frac{1}{Pr}\right)\left(\sum_{o=2}^{p}\sum_{k=0}^{o-2} b_o\,\chi_{o,k,2}\,\eta_q^{o-k-2}\right)+\left(\sum_{o=0}^{p} a_o\,\mathrm{VL}_o^s(\eta_q)\right)\left(\sum_{o=1}^{p}\sum_{k=0}^{o-1} b_o\,\chi_{o,k,1}\,\eta_q^{o-k-1}\right)-\left(\sum_{o=0}^{p} b_o\,\mathrm{VL}_o^s(\eta_q)\right).$$
$$\left(\sum_{o=1}^{p}\sum_{k=0}^{o-1} a_o\,\chi_{o,k,1}\,\eta_q^{o-k-1}\right)+Nt\left(\sum_{o=1}^{p}\sum_{k=0}^{o-1} b_o\,\chi_{o,k,1}\,\eta_q^{o-k-1}\right)^2+Nb\left(\sum_{o=1}^{p}\sum_{k=0}^{o-1} b_o\,\chi_{o,k,1}\,\eta_q^{o-k-1}\right).$$
$$\left(\sum_{o=1}^{p}\sum_{k=0}^{o-1} c_o\,\chi_{o,k,1}\,\eta_q^{o-k-1}\right)+Ec\left(\left(\sum_{o=2}^{p}\sum_{k=0}^{o-2} a_o\,\chi_{o,k,2}\,\eta_q^{o-k-2}\right)^2+\frac{W_e}{2}\left(\sum_{o=2}^{p}\sum_{k=0}^{o-2} a_o\,\chi_{o,k,2}\,\eta_q^{o-k-2}\right)^3\right).$$
$$\mathrm{Exp}\left(-\alpha\left(\sum_{o=0}^{p} b_o\,\mathrm{VL}_o^s(\eta_q)\right)\right)+Q\left(\sum_{o=0}^{p} b_o\,\mathrm{VL}_o^s(\eta_q)\right)=0. \tag{22}$$

$$\sum_{o=2}^{p}\sum_{k=0}^{o-2} c_o\,\chi_{o,k,2}\,\eta_q^{o-k-2} + Sc\left(\sum_{o=0}^{p} a_o\,\mathrm{VL}_o^{s}(\eta_q)\right)\left(\sum_{o=1}^{p}\sum_{k=0}^{o-1} c_o\,\chi_{o,k,1}\,\eta_q^{o-k-1}\right) + \frac{Nt}{Nb}\left(\sum_{o=2}^{p}\sum_{k=0}^{o-2} b_o\,\chi_{o,k,2}\,\eta_q^{o-k-2}\right) = 0. \tag{23}$$

Also, by substituting from Eq. (17) through the boundary conditions (13)–(14), it will be expressed in the following equations:

$$\sum_{o=0}^{p} 2(-1)^o\,a_o = \gamma, \qquad \sum_{o=0}^{p} 2(-1)^o\,b_o = 1, \qquad \sum_{o=0}^{p} 2(-1)^o\,c_o = 1, \tag{24}$$

$$\sum_{o=0}^{p} a_o\,\mathrm{VL}_o^{s'}(0) - \lambda\left(\sum_{o=0}^{p} a_o\,\mathrm{VL}_o^{s''}(0) + 0.5\,W_e\left(\sum_{o=0}^{p} a_o\,\mathrm{VL}_o^{s''}(0)\right)^2\right) \mathrm{Exp}\left(-\alpha\sum_{o=0}^{p} 2(-1)^o b_o\right) = 1, \tag{25}$$

$$\sum_{o=0}^{p} a_o\,\mathrm{VL}_o^{s'}(\hbar) = 0, \qquad \sum_{o=0}^{p} 2b_o = 0, \qquad \sum_{o=0}^{p} 2c_o = 0. \tag{26}$$

With the help of the following cost functions (CFs), the previous system defined in (21)–(26) can be expressed as a constrained optimization problem as follows:

$$\begin{aligned} CF1 = \sum_{q=0}^{p}\Bigg|&\left(1 + W_e\left(\sum_{o=2}^{p}\sum_{k=0}^{o-2} a_o\,\chi_{o,k,2}\,\eta_q^{o-k-2}\right)\right)\left(\sum_{o=3}^{p}\sum_{k=0}^{o-3} a_o\,\chi_{o,k,3}\,\eta_q^{o-k-3}\right) \\ &- \alpha\left(\sum_{o=1}^{p}\sum_{k=0}^{o-1} b_o\,\chi_{o,k,1}\,\eta_q^{o-k-1}\right).\left(\sum_{o=2}^{p}\sum_{k=0}^{o-2} a_o\,\chi_{o,k,2}\,\eta_q^{o-k-2}\right)\left(1 + 0.5W_e\left(\sum_{o=2}^{p}\sum_{k=0}^{o-2} a_o\,\chi_{o,k,2}\,\eta_q^{o-k-2}\right)\right) \\ &+ \left(\left(\sum_{o=0}^{p} a_o\,\mathrm{VL}_o^{s}(\eta_q)\right).\left(\sum_{o=2}^{p}\sum_{k=0}^{o-2} a_o\,\chi_{o,k,2}\,\eta_q^{o-k-2}\right) - 2\left(\sum_{o=1}^{p}\sum_{k=0}^{o-1} a_o\,\chi_{o,k,1}\,\eta_q^{o-k-1}\right)^2 - M\sin^2\beta.\right. \\ &\left.\left(\sum_{o=1}^{p}\sum_{k=0}^{o-1} a_o\,\chi_{o,k,1}\,\eta_q^{o-k-1}\right)\right).\mathrm{Exp}\left(\alpha\left(\sum_{o=0}^{p} b_o\,\mathrm{VL}_o^{s}(\eta_q)\right)\right) - K\left(\sum_{o=1}^{p}\sum_{k=0}^{o-1} a_o\,\chi_{o,k,1}\,\eta_q^{o-k-1}\right)\Bigg|, \end{aligned} \tag{27}$$

$$CF2 = \sum_{q=0}^{p} \Big| \Big(\frac{1}{Pr}\Big) \Bigg(\sum_{o=2}^{p} \sum_{k=0}^{o-2} b_o \, \chi_{o,k,2} \, \eta_q^{o-k-2} \Bigg) + \Bigg(\sum_{o=0}^{p} a_o \, \mathrm{VL}_o^s(\eta_q) \Bigg) \Bigg(\sum_{o=1}^{p} \sum_{k=0}^{o-1} b_o \, \chi_{o,k,1} \, \eta_q^{o-k-1} \Bigg)$$
$$- \Bigg(\sum_{o=0}^{p} b_o \, \mathrm{VL}_o^s(\eta_q) \Bigg) . \Bigg(\sum_{o=1}^{p} \sum_{k=0}^{o-1} a_o \, \chi_{o,k,1} \, \eta_q^{o-k-1} \Bigg) + Nt \Bigg(\sum_{o=1}^{p} \sum_{k=0}^{o-1} b_o \, \chi_{o,k,1} \, \eta_q^{o-k-1} \Bigg)^2$$
$$+ Nb \Bigg(\sum_{o=1}^{p} \sum_{k=0}^{o-1} b_o \, \chi_{o,k,1} \, \eta_q^{o-k-1} \Bigg) . \Bigg(\sum_{o=1}^{p} \sum_{k=0}^{o-1} c_o \, \chi_{o,k,1} \, \eta_q^{o-k-1} \Bigg) + Ec \Bigg(\Bigg(\sum_{o=2}^{p} \sum_{k=0}^{o-2} a_o \, \chi_{o,k,2} \, \eta_q^{o-k-2} \Bigg)^2$$
$$+ \frac{W_e}{2} \Bigg(\sum_{o=2}^{p} \sum_{k=0}^{o-2} a_o \, \chi_{o,k,2} \, \eta_q^{o-k-2} \Bigg)^3 \Bigg) \mathrm{Exp} \Bigg(-\alpha \Bigg(\sum_{o=0}^{p} b_o \, \mathrm{VL}_o^s(\eta_q) \Bigg) \Bigg) + Q \Bigg(\sum_{o=0}^{p} b_o \, \mathrm{VL}_o^s(\eta_q) \Bigg) \Big|, \tag{28}$$

$$CF3 = \sum_{q=0}^{p} \Big| \sum_{o=2}^{p} \sum_{k=0}^{o-2} c_o \, \chi_{o,k,2} \, \eta_q^{o-k-2} + Sc \Bigg(\sum_{o=0}^{p} a_o \, \mathrm{VL}_o^s(\eta_q) \Bigg) \Bigg(\sum_{o=1}^{p} \sum_{k=0}^{o-1} c_o \, \chi_{o,k,1} \, \eta_q^{o-k-1} \Bigg)$$
$$+ \frac{Nt}{Nb} \Bigg(\sum_{o=2}^{p} \sum_{k=0}^{o-2} b_o \, \chi_{o,k,2} \, \eta_q^{o-k-2} \Bigg) \Big|, \tag{29}$$

with the constraints (Cons):

$$\mathrm{Cons} = \Big| \sum_{o=0}^{p} 2(-1)^o \, a_o - \gamma \Big| + \sum_{o=0}^{p} 2(-1)^o \, b_o - 1 \Big| + \Big| \sum_{o=0}^{p} 2(-1)^o \, c_o - 1 \Big|$$
$$+ \Big| \sum_{o=0}^{p} a_o \, \mathrm{VL}_o^{s'}(0) - \lambda \Bigg(\sum_{o=0}^{p} a_o \, \mathrm{VL}_o^{s''}(0) + 0.5 \, W_e \Bigg(\sum_{o=0}^{p} a_o \, \mathrm{VL}_o^{s''}(0) \Bigg)^2 \Bigg) \mathrm{Exp} \Bigg(-\alpha \sum_{o=0}^{p} 2(-1)^o b_o \Bigg) - 1 \Big|$$
$$+ \Big| \sum_{o=0}^{p} a_o \, \mathrm{VL}_o^{s'}(\hbar) \Big| + \Big| \sum_{o=0}^{p} 2b_o \Big| + \Big| \sum_{o=0}^{p} 2c_o \Big| . \tag{30}$$

The constrained optimization problem (27)–(30) can be solved by using the Penalty Leap Frog procedure [21] for the coefficients a_o, b_o, c_o, , $o = 0, 1, \ldots, p$. This in turn leads us to formulate the approximate solution by substitution in the form (17).

Table 1 Comparison of $\sqrt{2} Cf_x \mathrm{Re}_x^{1/2}$ for different values of W_e and γ with the results [22] when $\alpha = K = M = \lambda = 0$

W_e	γ	Nadeem and Hussain [22]	Present work
0.0	0.0	1.28180	1.2817990018
0.1	0.0	1.25153	1.2515288741
0.2	0.0	1.21794	1.2179388149
0.3	0.0	1.17956	1.1795598410
0.0	0.2	1.19298	1.1929772090
0.1	0.2	1.16468	1.1646759198
0.2	0.2	1.13365	1.1336479985
0.3	0.2	1.09881	1.0988075120

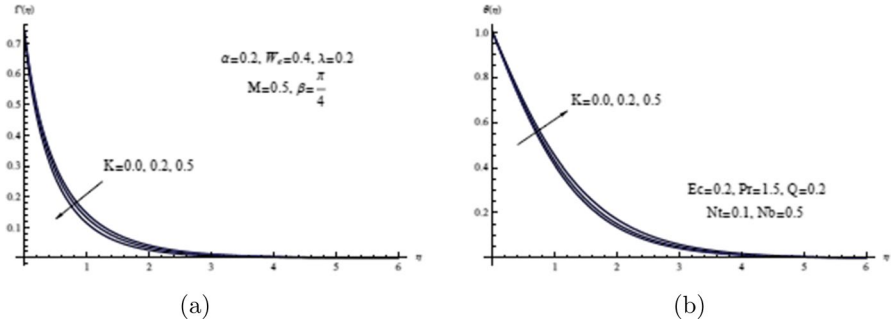

Fig. 2 **a** Velocity $f'(\eta)$ for different K **b** Temperature $\theta(\eta)$ for different K

6 Results and Discussion

We have determined the approximate values by using the Vieta-Lucas collocation method for the SFC, and compared them with those values of Nadeem and Hussain [22] in Table 1 to confirm the accuracy of our numerical solutions with the order of approximation $p = 6$. These numerical solutions estimate the skin friction coefficient was calculated using the identical parametric data from both investigations, pointing to the same circumstance in both. We see that the comparison demonstrates good agreement. In light of this, we are certain that the data shown here are quite accurate.

Figure 2 shows the effect of K on graphs of $f'(\eta)$ and $\theta(\eta)$. The temperature distribution is seen to be improved by an increase in K, whereas the velocity field shows the opposite tendency. The existence of porous media is a flow resistance mechanism, hence the observed behavior in the velocity field is expected. Here and all figures, we take the order of approximation $p = 7$, and the interval (0,6).

Figure 3 illustrates the graphical output of $f'(\eta)$ and $\theta(\eta)$ profiles for different values of the parameter β. The Williamson nanofluid flow speed $f'(\eta)$ is confirmed to be at its highest when the inclination angle β is minimal by the

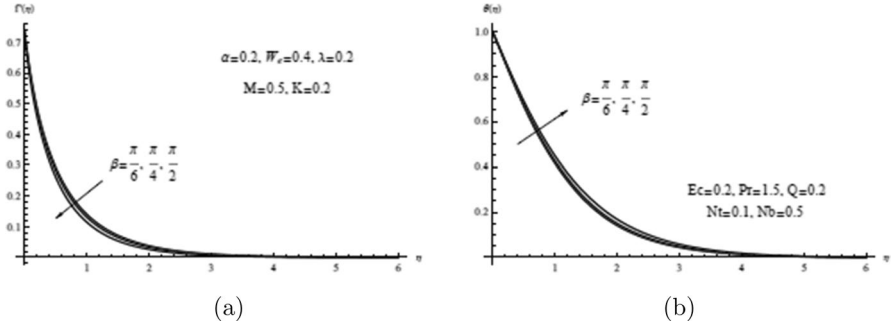

Fig. 3 **a** Velocity $f'(\eta)$ for different β **b** Temperature $\theta(\eta)$ for different β

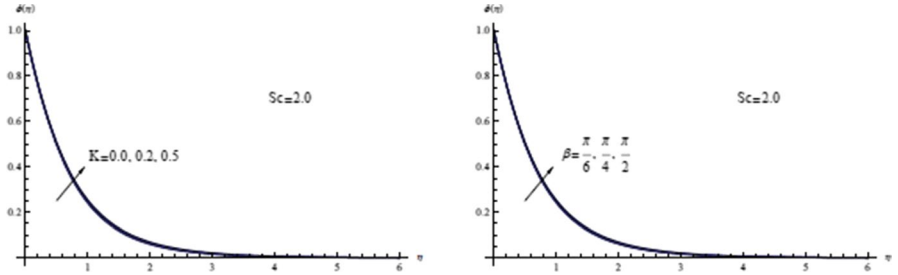

(a) Concentration $\phi(\eta)$ for different K (b) Concentration $\phi(\eta)$ for different β

Fig. 4 **a** Concentration $\phi(\eta)$ for different K **b** Concentration $\phi(\eta)$ for different β

discovery that the velocity decreases with increasing β. Likewise, it has been shown that when the inclination angle β is at its highest, a minor increase in temperature behavior $\theta(\eta)$ occurs more quickly. Additionally, it is obvious that with greater values of β, the temperature boundary layer thickens.

To see how the porous K and the aligned magnetic field angle β parameters affect the concentration $\phi(\eta)$ of the Williamson nanofluid, look at Fig. 4. The graph makes it clear that the magnetic field's inclination angle and the porosity parameter's strength can be used to gently alter the concentration of nanoparticles.

The distributions of $f'(\eta)$ and $\theta(\eta)$ are examined concerning the similarity variable η for different values of λ in Fig. 5. For lower values of λ, enhancement behavior is seen in both the $f'(\eta)$ and $\theta(\eta)$ fields. The thinned boundary layer that results from the action of the slip velocity phenomena is advantageous to the stability of the nanofluid flow, it is inferred. Additionally, this decrease in temperature distribution caused by the slip velocity phenomenon may be advantageous for cooling procedures, which are crucial in several engineering applications.

The distributions of $f'(\eta)$ and $\theta(\eta)$ are given in Fig. 6 for various quantities of M. It is revealed that shear stress increases for larger magnetic parameter quantities, which causes a decrease in the nanofluid velocity field. It is true physically because

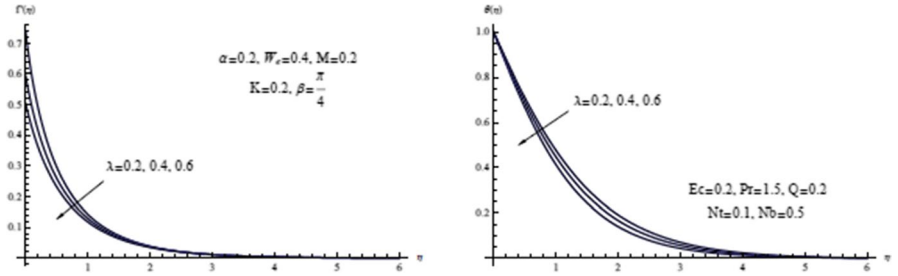

(a) Velocity $f'(\eta)$ for different λ (b) Temperature $\theta(\eta)$ for different λ

Fig. 5 **a** Velocity $f'(\eta)$ for different λ **b** Temperature $\theta(\eta)$ for different λ

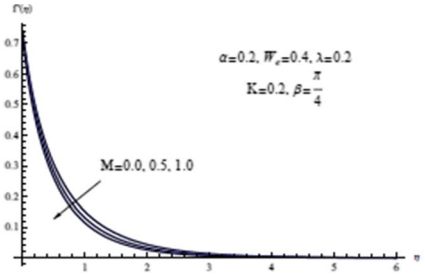

(a) Velocity $f'(\eta)$ for different M

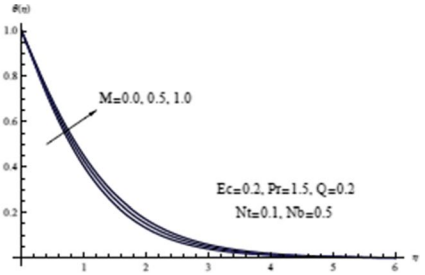

(b) Temperature $\theta(\eta)$ for different M

Fig. 6 **a** Velocity $f'(\eta)$ for different M **b** Temperature $\theta(\eta)$ for different M

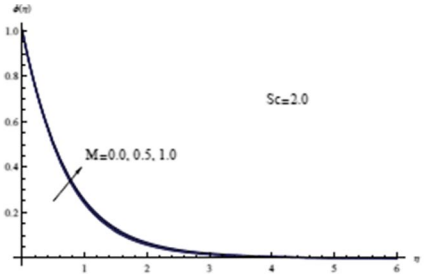

(a) Concentration $\phi(\eta)$ for different M

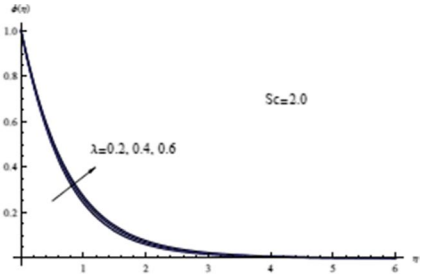

(b) Concentration $\phi(\eta)$ for different λ

Fig. 7 **a** Concentration $\phi(\eta)$ for different M **b** Concentration $\phi(\eta)$ for different λ

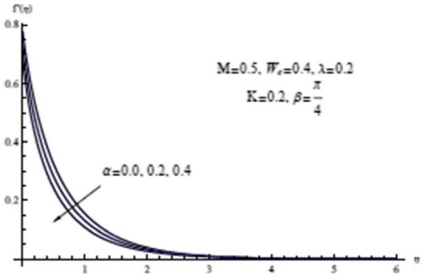

(a) Velocity $f'(\eta)$ for different α

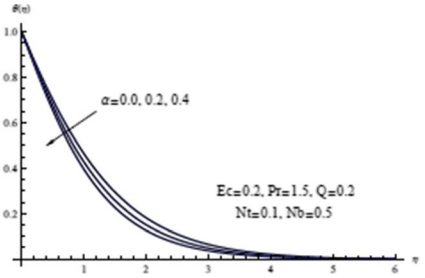

(b) Temperature $\theta(\eta)$ for different α

Fig. 8 **a** Velocity $f'(\eta)$ for different α **b** Temperature $\theta(\eta)$ for different α

when the intensity of the Lorentz force grows with an increase in M, the nanofluid flow is physically resisted more and as a result, velocity diminished. This declining tendency in the velocity profile also suggests that as M is elevated, the thickness of the BL shrinks. Further, the $\theta(\eta)$-field shows a different pattern as the magnetic

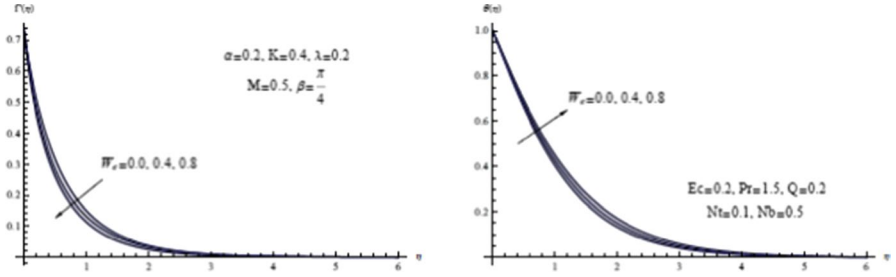

(a) Velocity $f'(\eta)$ for different W_e (b) Temperature $\theta(\eta)$ for different W_e

Fig. 9 **a** Velocity $f'(\eta)$ for different W_e **b** Temperature $\theta(\eta)$ for different W_e

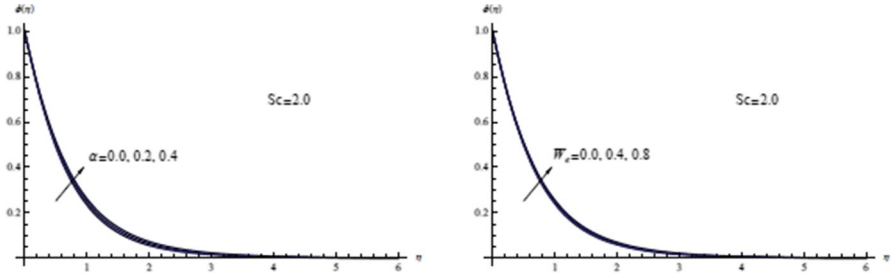

(a) Concentration $\phi(\eta)$ for different α (b) Concentration $\phi(\eta)$ for different W_e

Fig. 10 **a** Concentration $\phi(\eta)$ for different α **b** Concentration $\phi(\eta)$ for different W_e

parameter is raised, indicating that the resistive force can assist raise both the thermal thickness and the temperature of the nanofluid.

The behavior of the magnetic M and the slip velocity λ parameters concerning the concentration of nanoparticles is explained in Fig. 7. This graph confirms that both M and λ have a minimal impact on the profiles of nanoparticle concentration and that this consequence also contributes to a small improvement in boundary layer thickness.

For distinct quantities of α, Fig. 8 is carefully examined to communicate deviations in $f'(\eta)$ and $\theta(\eta)$ profiles. In the BL region, both velocity and temperature profiles exhibit an evidently declining tendency. This is completely true since higher viscosity parameter values lead to greater shear stress, which restricts the motion of the nanofluid.

Figure 9 displays $f'(\eta)$ and $\theta(\eta)$ profiles for a few Williamson parameter W_e values that describe the flow behavior and the heat transfer distribution through the BL. Here, increasing W_e causes the velocity profile to degrade dramatically, although the $\theta(\eta)$-field shows the opposite tendency. As a result of the large shear stress caused by the great W_e, which creates a flow resistance mechanism for the nonfluid motion, it is to be expected.

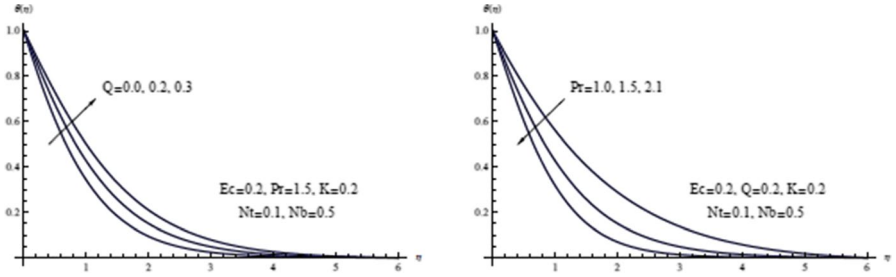

(a) Temperature $\theta(\eta)$ for different Q (b) Temperature $\theta(\eta)$ for different Pr

Fig. 11 **a** Temperature $\theta(\eta)$ for different Q **b** Temperature $\theta(\eta)$ for different Pr

The behavior of the Williamson and viscosity parameters on the nanofluid concentration field is illustrated in Fig. 10. This graphic shows how increasing either the Williamson parameter or the viscosity parameter will result in a modest enhancement in the concentration of nanofluid.

The effect of Q on the Williamson nanofluid flow's $\theta(\eta)$-distribution is depicted in Fig. 11a. This graph demonstrates how the temperature profile rises when Q is raised. Because boosting the values of the heat source parameter results in an improvement in the internal heat capacity of the nanofluid, which raises the $\theta(\eta)$ -distribution. Following that, Fig. 11b illustrates Pr varying on the $\theta(\eta)$-field. This graph demonstrates that a decrease in $\theta(\eta)$-distribution results from an increase in the Prandtl number. Temperature decreases as a result of reduced thermal diffusivity caused by an increase in Pr.

Figure 12a plots the variation of $\theta(\eta)$ with Ec. It has been noted that the temperature profile exhibits rising behavior for high Eckert numbers. The reason for this is that a higher Ec improves the kinetic energy that is converted to thermal energy, which raises both θ-distribution and the thickness of the thermal BL. Further, Fig. 12b examines how the parameter Nb impacts the $\theta(\eta)$-profile. It has been discovered that raising Nb improves the $\theta(\eta)$-profile. The additional

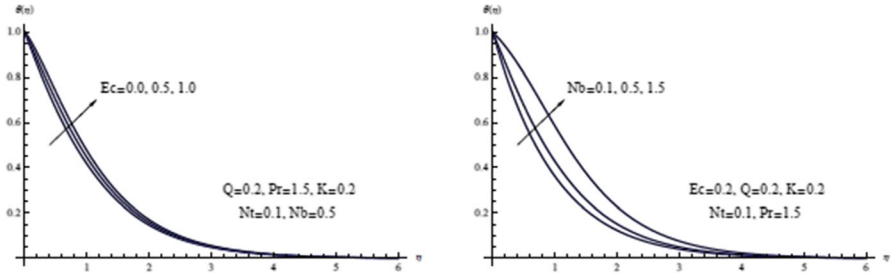

(a) Temperature $\theta(\eta)$ for different Ec (b) Temperature $\theta(\eta)$ for different Nb

Fig. 12 **a** Temperature $\theta(\eta)$ for different Ec **b** Temperature $\theta(\eta)$ for different Nb

Table 2 Values for the REF in the current method

η	REF of $f(\eta)$	REF of $\theta(\eta)$	REF of $\phi(\eta)$
0.0	3.741258E-06	5.852460E-07	3.854623E-08
1.0	1.852321E-07	8.654123E-06	4.852147E-07
2.0	4.951753E-07	3.951789E-06	0.963258E-07
3.0	0.620147E-08	0.652103E-07	8.951753E-07
4.0	2.012453E-07	2.012345E-07	7.654123E-08
5.0	5.854697E-07	4.014785E-08	1.954879E-07
6.0	2.963147E-08	2.320145E-07	7.621001E-06

random movement for nanoparticles caused by an increase in the parameter *Nb* aids in transmitting heat through the boundary layer, which raises the temperature distribution.

To validate the accuracy of the approximation method, we evaluated through Table 2 the residual error function (REF) [23] of the current method with the values of parameters $W_e = 0.4$, $\alpha = K = Ec = Q = \lambda = 0.2$, $M = Nb = 0.5$, $\beta = \frac{\pi}{4}$, $Pr = 1.5$, $Nt = 0.1$, $Sc = 2.0$ and $p = 8$. These values show the thoroughness of the proposed method in this article and confirm that the current method gives better accuracy.

Finally, in Table 3 (with $p = 7$), we present an adjustment of SFC, LNN and, LSN against various embedded factors. It is important to keep in mind that the local SFC decreases as slip velocity, Williamson, heat source, and Eckert number values increase, but that this effect is reversed for high values of the porous parameter, Prandtl number, aligned magnetic field angle, magnetic number, and viscosity parameter. The table also makes clear that the local Sherwood number values decline when the porous parameter, aligned magnetic field angle, λ, α, and M values rise, whereas the opposite direction is seen for the Eckert number and heat source parameter. Finally, a further examination of this table reveals that the local Nusselt number is strongly subject to a lowering tendency when K, λ, M, and α are included, whereas the Prandtl number exhibits the opposite trend.

7 Conclusions

We have developed the approximate solutions for the proposed model by using the given method. The impacts of thermophoresis, viscous dissipation, Brownian motion, and slip velocity are all joined into the nanofluid system. Creating a justification for the heat transfer improvement seen in non-Newtonian Williamson nanofluids was the aim of this research. The relationship between physical variables and alterations in f', θ, ϕ, the skin-friction coefficient, the Sherwood number, and the Nusselt number is examined using tables and diagrams. The following list includes significant findings from the current analysis.

Table 3 Values of $\sqrt{2}Cf_x\mathrm{Re}_x^{1/2}$, $\frac{1}{\sqrt{2}}\mathrm{Re}_x^{-1/2}e^{\frac{-x}{2L}}Nu_x$ and $\frac{1}{\sqrt{2}}\mathrm{Re}_x^{-1/2}e^{\frac{-x}{2L}}Sh_x$ for distinct quantities of K, β, λ, W_e, M, α, Nb, Q and Ec with $Nt = 0.1$

K	β	λ	M	α	W_e	Q	Pr	Ec	$-\left(f''(0)+\frac{W_e}{2}f''^2(0)\right)e^{-\alpha\theta(0)}$	$-\theta'(0)$	$-\phi'(0)$
0.0	$\frac{\pi}{4}$	0.2	0.5	0.2	0.4	0.2	1.5	0.2	1.31393521	0.719235314	1.3191615
0.2	$\frac{\pi}{4}$	0.2	0.5	0.2	0.4	0.2	1.5	0.2	1.34424013	0.690293912	1.3084528
0.5	$\frac{\pi}{4}$	0.2	0.5	0.2	0.4	0.2	1.5	0.2	1.38388091	0.650636985	1.2946420
0.2	$\frac{\pi}{6}$	0.2	0.5	0.2	0.4	0.2	1.5	0.2	1.32242501	0.710233025	1.3158550
0.2	$\frac{\pi}{4}$	0.2	0.5	0.2	0.4	0.2	1.5	0.2	1.34424013	0.690293912	1.3084528
0.2	$\frac{\pi}{2}$	0.2	0.5	0.2	0.4	0.2	1.5	0.2	1.38328521	0.652823974	1.2952402
0.2	$\frac{\pi}{4}$	0.2	0.5	0.2	0.4	0.2	1.5	0.2	1.34424013	0.690293912	1.3084528
0.2	$\frac{\pi}{4}$	0.4	0.5	0.2	0.4	0.2	1.5	0.2	1.01534921	0.664541017	1.2690992
0.2	$\frac{\pi}{4}$	0.6	0.5	0.2	0.4	0.2	1.5	0.2	0.82633920	0.617818952	1.2359791
0.2	$\frac{\pi}{4}$	0.2	0.0	0.2	0.4	0.2	1.5	0.2	1.29883012	0.731135911	1.3238978
0.2	$\frac{\pi}{4}$	0.2	0.5	0.2	0.4	0.2	1.5	0.2	1.34424013	0.690293912	1.3084528
0.2	$\frac{\pi}{4}$	0.2	1.0	0.2	0.4	0.2	1.5	0.2	1.38328910	0.652824851	1.2952401
0.2	$\frac{\pi}{4}$	0.2	0.5	0.0	0.4	0.2	1.5	0.2	1.11884921	0.736679021	1.3434290
0.2	$\frac{\pi}{4}$	0.2	0.5	0.2	0.4	0.2	1.5	0.2	1.34424013	0.690293912	1.3084528
0.2	$\frac{\pi}{4}$	0.2	0.5	0.4	0.4	0.2	1.5	0.2	1.57225952	0.637652951	1.2744501
0.2	$\frac{\pi}{4}$	0.2	0.5	0.2	0.0	0.2	1.5	0.2	1.43988036	0.729129214	1.3253402
0.2	$\frac{\pi}{4}$	0.2	0.5	0.2	0.4	0.2	1.5	0.2	1.34424013	0.690293912	1.3084528
0.2	$\frac{\pi}{4}$	0.2	0.5	0.2	0.8	0.2	1.5	0.2	1.33312098	0.650636021	1.2946490
0.2	$\frac{\pi}{4}$	0.2	0.5	0.2	0.4	0.0	1.5	0.2	1.38431147	0.882162720	1.2712391
0.2	$\frac{\pi}{4}$	0.2	0.5	0.2	0.4	0.2	1.5	0.2	1.34424013	0.690293912	1.3084528
0.2	$\frac{\pi}{4}$	0.2	0.5	0.2	0.4	0.3	1.5	0.2	1.31613925	0.554733521	1.3344890
0.2	$\frac{\pi}{4}$	0.2	0.5	0.2	0.4	0.2	1.0	0.2	1.30721085	0.513499010	1.3431211
0.2	$\frac{\pi}{4}$	0.2	0.5	0.2	0.4	0.2	1.5	0.2	1.34424013	0.690293912	1.3084528

Table 3 (continued)

K	β	λ	M	α	W_e	Q	Pr	Ec	$-\left(f''(0)+\frac{W_e}{2}f''^2(0)\right)e^{-\alpha\theta(0)}$	$-\theta'(0)$	$-\phi'(0)$
0.2	$\frac{\pi}{4}$	0.2	0.5	0.2	0.4	0.2	2.1	0.2	1.37791025	0.848626512	1.2787691
0.2	$\frac{\pi}{4}$	0.2	0.5	0.2	0.4	0.2	1.5	0.0	1.36168158	0.776825810	1.2909291
0.2	$\frac{\pi}{4}$	0.2	0.5	0.2	0.4	0.2	1.5	0.5	1.34424013	0.690293912	1.3084528
0.2	$\frac{\pi}{4}$	0.2	0.5	0.2	0.4	0.2	1.5	1.0	1.27234935	0.326666032	1.3821813

1. When the heat source, slip velocity, and Williamson parameters are enhanced, the skin friction falls.
2. The two most significant processes for nanoparticle/base-fluid slip have been identified as Brownian diffusion and thermophoresis.
3. It is possible to control a process temperature using λ and α parameters.
4. When K, γ, α, M, and λ are increased, the velocity and momentum boundary layer also decline.
5. The Sherwood number has increased as Ec and Q improve, whereas it drops as the slip velocity, viscosity, and porous parameter boosts.
6. The value of heat transmission drops as K and α values improve, and it grows as the Prandtl number rises.
7. Slip velocity and greater levels of the viscosity parameter are two factors that regulate the temperature of nanofluids.

Acknowledgements The authors extend their appreciation to the Deanship of Scientific Research, Imam Mohammad Ibn Saud Islamic University (IMSIU), Saudi Arabia, for funding this research work through Grant No. (221412018).

Declarations

Conflict of interest The authors declare that they have no conflicts of interest.

References

1. Williamson, R.V.: The flow of pseudo-plastic materials. Ind. Eng. Chem. **21**, 1108–1111 (1929)
2. Dapra, I., Scarpi, G.: Perturbation solution for the pulsatile flow of a non-Newtonian Williamson fluid in a rock fracture. Int. J. Rock Mech. Min. Sci. **44**, 271–278 (2007)
3. Nadeem, S., Hussain, S.T.: Flow and heat transfer analysis of Williamson nanofluid. Appl. Nanosci. **4**, 1005–1012 (2014)
4. Nadeem, S., Hussain, S.T.: Analysis of MHD Williamson nano fluid flow over a heated surface. J. Appl. Fluid Mech. **9**, 729–739 (2016)
5. Choi, S.U.S., Zhang, Z.G., Yu, W., Lockwood, F.E., Grulke, E.A.: Anomalous thermal conductivity enhancement in nanotube suspensions. Applied Physics Letters **79**, 2252–2254 (2001)
6. Khan, W.A., Pop, I.: Boundary-layer flow of a nanofluid past a stretching sheet. Int. J. Heat Mass Trans. **53**, 2477–2483 (2010)
7. Khan, M., Malik, M.Y., Salahuddin, T., Rehman, K.U., Naseer, M., Khan, I.: Numerical study for MHD peristaltic flow of Williamson nanofluid in an endoscope with partial slip and Journal wall properties. International of Heat and Mass Transfer **114**, 1181–1187 (2017)
8. Krishnamurthy, M.R., Prassanakumara, B.C., Gireesha, B.J., Gorla, R.S.R.: Effect of chemical reaction on MHD boundary layer flow and melting heat transfer of Williamson nanofluid in a porous medium. Engineering Science and Technology: An International Journal **19**, 53–61 (2016)
9. Choi, U.S.: Enhancing thermal conductivity of fluids with nanoparticles. ASME FED **231**, 99–103 (1995)

10. Muthtamilselvan, M., Kandaswamy, P., Lee, J.: Heat transfer enhancement of copper-water nanofluids in a lid-driven enclosure. Commun. Nonlinear Sci. Numer. Simulat. **15**, 1501–1510 (2010)
11. Ramesh, G.K., Roopa, G.S., Gireesha, B.J., Shehzad, S.A., Abbasi, F.M.: An electro-magneto-hydrodynamic flow Maxwell nanoliquid past a Riga plate: a numerical study. J Braz. Soc. Mech. Sci. Eng. **39**, 4547–4554 (2017)
12. Yousef, N.S., Megahed, A.M., Ghoneim, N.I., Elsafi, M., Fares, E.: Chemical reaction impact on MHD dissipative Casson-Williamson nanofluid flow over a slippery stretching sheet through a porous medium. Alexandria Engineering Journal **61**, 10161–10170 (2022)
13. Khader, M.M.: Mittag-Leffler collocation optimization method for studying a physical problem in fluid flow with fractional derivatives. Mathematical Methods in the Applied Sciences **12**, 1–18 (2021)
14. Khader, M.M., Ahmed, M.: Megahed, Approximate solutions for the flow and heat transfer due to a stretching sheet embedded in a porous medium with variable thickness, variable thermal conductivity, and thermal radiation using Laguerre collocation method. Applications and Applied Mathematics: An International Journal **10**, 817–834 (2015)
15. Khader, M.M.: Numerical study for unsteady Casson fluid flow with heat flux using a spectral collocation method. Indian Journal of Physics **96**, 777–786 (2021)
16. Khader, M.M., Babatin, M.M., Megahed, Ahmed M., Eid, A.: Implementing the Galerkin method associated with the shifted Vieta-Lucas polynomials for studying numerically the bio-nanofluid flow which is saturated by gyrotactic microorganisms over a slippery stretching sheet. Journal of Mathematics 2022, 1-15 (2022)
17. Zakaria, M., Khader, M.M., Al-Dayel, Ibrahim, Al-Tayeb, W.: Solving fractional generalized Fisher-Kolmogorov-Petrovsky-Piskunov's equation using compact finite different method together with spectral collocation algorithms. Journal of Mathematics 2022, 1-9 (2022)
18. Li, Yi-Xia, Mohammed, H.A., Yu-Pei, Lv., Ilyas, K., Riaz, K.M., Issakhov, A.: Heat and mass transfer in MHD Williamson nanofluid flow over an exponentially porous stretching surface. Case Studies in Thermal Engineering **26**, 100975 (2021)
19. Megahed, A.M.: Improvement of heat transfer mechanism through a Maxwell fluid flow over a stretching sheet embedded in a porous medium and convectively heated. Mathematics and Computers in Simulation **187**, 97–109 (2021)
20. Nadeem, S., Hussain, S.T., Lee, C.: Flow of a Williamson fluid over a stretching sheet. Braz. J. Chem. Eng. **30**, 619–625 (2013)
21. El-Hawary, H.M., Salim, M.S., Hussien, H.S.: Ultraspherical integral method for optimal control problems governed by ordinary differential equations. J. Glob. Optim. **25**, 283–303 (2003)
22. Nadeem, S., Hussain, S.T.: Heat transfer analysis of Williamson fluid over exponentially stretching surface. Appl. Math. Mech.-Engl. Ed. **35**, 489–502 (2014)
23. Khader, M.M., Saad, K.M.: On the numerical evaluation for studying the fractional KdV, KdV-Burger's, and Burger's equations. The European Physical Journal Plus **133**, 1–13 (2018)